**PAPER • OPEN ACCESS**

# Overview of physics results from MAST upgrade towards core-pedestal-exhaust integration

View the article online for updates and enhancements.

# Overview of physics results from MAST upgrade towards core-pedestal-exhaust integration

J.R. Harrison[1,*], A. Aboutaleb[2], S. Ahmed[3], M. Aljunid[1], S.Y. Allan[1], H. Anand[4], Y. Andrew[5], L.C. Appel[1], A. Ash[1], J. Ashton[1], O. Bachmann[1], M. Barnes[6], B. Barrett[1], D. Baver[7], D. Beckett[1], J. Bennett[1], J. Berkery[8], M. Bernert[9], W. Boeglin[2], C. Bowman[1], J. Bradley[10], D. Brida[9], P.K. Browning[11], D. Brunetti[1], P. Bryant[10], J. Bryant[10], J. Buchanan[1], N. Bulmer[1], A. Carruthers[1], L. Casali[12], M. Cecconello[13], Z.P. Chen[14], J. Clark[1,10], C. Cowley[15], M. Coy[1], N. Crocker[16], G. Cunningham[1], I. Cziegler[15], T. Da Assuncao[1], Y. Damizia[10], P. Davies[1], I.E. Day[1], G.L. Derks[17,18], S. Dixon[1], R. Doyle[19], M. Dreval[20], M. Dunne[9], B.P. Duval[21], T. Eagles[1], J. Edmond[1], H. El-Haroun[1], S.D. Elmore[1], Y. Enters[15], M. Faitsch[9], F. Federici[22], N. Fedorczak[23], F. Felici[21], A.R. Field[1], M. Fitzgerald[1], I. Fitzgerald[1], R. Fitzpatrick[14], L. Frassinetti[24], W. Fuller[25], D. Gahle[26], J. Galdon-Quiroga[27], L. Garzotti[1], S. Gee[1], T. Gheorghiu[15], S. Gibson[1], K.J. Gibson[15], C. Giroud[1], D. Greenhouse[15], V.H. Hall-Chen[28], C.J. Ham[1], R. Harrison[1], S.S. Henderson[1], C. Hickling[1,10], B. Hnat[25], L. Howlett[15], J. Hughes[29], R. Hussain[1], K. Imada[15], P. Jacquet[1], P. Jepson[1], B. Kandan[1], I. Katramados[1], Y.O. Kazakov[30], D. King[1], R. King[1], A. Kirk[1], M. Knolker[4], M. Kochan[1], L. Kogan[1], B. Kool[17,18], M. Kotschenreuther[14], K. -W. Lee[12], M. Lees[1], A.W. Leonard[4], G. Liddiard[1], B. Lipschultz[15], Y.Q. Liu[4], B.A. Lomanowski[22], N. Lonigro[15], J. Lore[22], J. Lovell[22], S. Mahajan[14], F. Maiden[15], C. Man-Friel[1], F. Mansfield[1], S. Marsden[1], R. Martin[1], S. Mazzi[21], R. McAdams[1], G. McArdle[1], K.G. McClements[1], J. McClenaghan[4], D. McConville[1], K. McKay[10], C. McKnight[1], P. McKnight[1], A. McLean[31], B.F. McMillan[25], A. McShee[1], J. Measures[1], N. Mehay[1], C.A. Michael[16], F. Militello[1], D. Morbey[1], S. Mordijck[32], D. Moulton[1], O. Myatra[1], A.O. Nelson[33], M. Nicassio[1], M.G. O'Mullane[26], H.J.C. Oliver[1], P. Ollus[34], T. Osborne[4], N. Osborne[10], E. Parr[1], B. Parry[1], B.S. Patel[1], D. Payne[1], C. Paz-Soldan[33], A. Phelps[26], L. Piron[35,36], C. Piron[37], G. Prechel[38], M. Price[1], B. Pritchard[15], R. Proudfoot[1], H. Reimerdes[21], T. Rhodes[16], P. Richardson[1], J. Riquezes[33], J.F. Rivero-Rodriguez[1], C.M. Roach[1], M. Robson[1], K. Ronald[26], E. Rose[1], P. Ryan[1], D. Ryan[1], S. Saarelma[1], S. Sabbagh[33], R. Sarwar[1], P. Saunders[1], O. Sauter[21], R. Scannell[1], T. Schuett[15], R. Seath[1], R. Sharma[1], P. Shi[1], B. Sieglin[9], M. Simmonds[1], J. Smith[1], A. Smith[1], V. A. Soukhanovskii[31], D. Speirs[26], G. Staebler[4], R. Stephen[1], P. Stevenson[1], J. Stobbs[1], M. Stott[1], C. Stroud[1], C. Tame[1], C. Theiler[21], N. Thomas-Davies[1], A.J. Thornton[1], M. Tobin[33], M. Vallar[21], R.G.L. Vann[15], L. Velarde[39], K. Verhaegh[1], E. Viezzer[27], C. Vincent[1], G. Voss[1], M. Warr[1], W. Wehner[4], S. Wiesen[40], T.A. Wijkamp[17,18], D. Wilkins[1], T. Williams[1], T. Wilson[1], H.R. Wilson[15,22], H. Wong[16], M. Wood[1] and V. Zamkovska[33]

[1] UKAEA (United Kingdom Atomic Energy Authority), Culham Science Centre, Abingdon, Oxfordshire OX14 3DB, United Kingdom of Great Britain and Northern Ireland
[2] Department of Physics, Florida International University, 11200 SW, Miami, FL 33199, United States of America

* Author to whom any correspondence should be addressed.

3 Department of Physics and Technology, UiT The Arctic University of Norway N-9037 Tromsø, Norway

4 General Atomics, PO Box 85608, San Diego, CA 92186-5608, United States of America

5 Blackett Laboratory, Imperial College London, London SW7 2BW, United Kingdom of Great Britain and Northern Ireland

6 Rudolf Peierls Centre for Theoretical Physics, University of Oxford, Oxford OX1 3NP, United Kingdom of Great Britain and Northern Ireland

7 Astrodel LLC, Boulder, CO 80303, United States of America

8 Princeton Plasma Physics Laboratory, Princeton, NJ, United States of America

9 Max-Planck-Institut fur Plasmaphysik 85748 Garching, Germany

10 Department of Electrical Engineering and Electronics, University of Liverpool, Brownlow Hill, Liverpool L69 3GJ, United Kingdom of Great Britain and Northern Ireland

11 Department of Physics and Astronomy, University of Manchester, Oxford Road, Manchester M13 9PL, United Kingdom of Great Britain and Northern Ireland

12 University of Tennessee, Knoxville, Knoxville, TN 37996, United States of America

13 Department of Physics, Durham University, Durham DH1 3LE, United Kingdom of Great Britain and Northern Ireland

14 Institute for Fusion Studies, The University of Texas at Austin, Austin, TX, United States of America

15 York Plasma Institute, Department of Physics, University of York, Heslington, York YO10 5DD, United Kingdom of Great Britain and Northern Ireland

16 Physics and Astronomy Department, University of California, Los Angeles, CA 90098, United States of America

17 Dutch Institute for Fundamental Energy Research DIFFER, Eindhoven, Netherlands

18 Eindhoven University of Technology, Eindhoven, Netherlands

19 Dublin City University, Dublin, Ireland

20 National Science Center 'Kharkov Institute of Physics and Technology', Akademichna 1, Kharkiv 61108, Ukraine

21 Ecole Polytechnique Fédérale de Lausanne (EPFL), Swiss Plasma Center (SPC) CH-1015 Lausanne, Switzerland

22 Oak Ridge National Laboratory, Oak Ridge, TN 37831, United States of America

23 CEA, IRFM F-13108 Saint-Paul-lez-Durance, France

24 Division of Fusion Plasma Physics, KTH Royal Institute of Technology, Stockholm SE-100 44, Sweden

25 Department of Physics, University of Warwick, Coventry CV4 7AL, United Kingdom of Great Britain and Northern Ireland

26 Department of Physics, SUPA, University of Strathclyde, Glasgow, Scotland, United Kingdom of Great Britain and Northern Ireland

27 Dpto. de Física Atómica, Molecular y Nuclear, Universidad de Sevilla 41012 Sevilla, Spain

28 IHPC, Agency for Science, Technology and Research (A*STAR), Singapore 138632, Singapore

29 Plasma Science and Fusion Center, Massachusetts Institute of Technology, Cambridge, MA 02139, United States of America

30 Laboratory for Plasma Physics, LPP-ERM/KMS, TEC Partner, Brussels, Belgium

31 Lawrence Livermore National Laboratory, Livermore, CA, United States of America

32 Department of Computer Science, College of William & Mary, Williamsburg, VA, United States of America

33 Department of Applied Physics and Applied Mathematics, Columbia University, New York, NY, United States of America

34 Department of Applied Physics, Aalto University, PO Box 11100 00076 Aalto, Finland

35 Dipartimento di Fisica 'G. Galilei', Università degli Studi di Padova, Padova, Italy

36 Consorzio RFX, Corso Stati Uniti 4 35127 Padova, Italy

37 ENEA, Fusion and Nuclear Safety Department, C. R. Frascati, Via E. Fermi 45 00044 Frascati, Roma, Italy

38 University of California Irvine, Irvine, CA 92697, United States of America

39 Dpto. de Ingeniería Energética, ETSI, Universidad de Sevilla 41092 Sevilla, Spain

40 Forschungszentrum Jülich GmbH, Institut für Energie- und Klimaforschung—Plasmaphysik 52425 Jülich, Germany

E-mail: James.Harrison@ukaea.uk

CrossMark

## Abstract

Recent results from MAST Upgrade are presented, emphasising understanding the capabilities of this new device and deepening understanding of key physics issues for the operation of ITER

and the design of future fusion power plants. The impact of MHD instabilities on fast ion confinement have been studied, including the first observation of fast ion losses correlated with Compressional and Global Alfvén Eigenmodes. High-performance plasma scenarios have been developed by tailoring the early plasma current ramp phase to avoid internal reconnection events, resulting in a more monotonic q profile with low central shear. The impact of $m/n = 3/2$, 2/1 and 1/1 modes on thermal plasma confinement and rotation profiles has been quantified, and scenarios optimised to avoid them have transiently reached values of normalised beta approaching 4.2. In pedestal and ELM physics, a maximum pedestal top temperature of $\sim$350 eV has been achieved, exceeding the value achieved on MAST at similar heating power. Mitigation of type-I ELMs with $n = 1$ RMPs has been observed. Studies of plasma exhaust have concentrated on comparing conventional and Super-X divertor configurations, while X-point target, X-divertor and snowflake configurations have been developed and studied in parallel. In L-mode discharges, the separatrix density required to detach the outer divertors is approximately a factor 2 lower in the Super-X than the conventional configuration, in agreement with simulations. Detailed analysis of spectroscopy data from studies of the Super-X configuration reveal the importance of including plasma-molecule interactions and $D_2$ Fulcher band emission to properly quantify the rates of ionisation, plasma-molecule interactions and volumetric recombination processes governing divertor detachment. In H-mode with conventional and Super-X configurations, the outer divertors are attached in the former and detached in the latter with no impact on core or pedestal confinement.

(Some figures may appear in colour only in the online journal)

## 1. Introduction and MAST upgrade capabilities

MAST Upgrade is a low aspect ratio tokamak (major radius $(R)$/minor radius $(a)$ = 0.85/0.65 $\sim$1.3, plasma current $(I_p) \leqslant 2.0$ MA, toroidal field on axis $(B_\varphi) \leqslant 0.8$ T, pulse length $< 5$ s) and one of the largest spherical tokamaks worldwide, together with NSTX-U [1]. A poloidal cross-section of MAST Upgrade is shown in figure 1. It has considerable flexibility to independently vary the shape of the plasma core and divertors within tightly baffled chambers utilising 22 poloidal field coils to facilitate optimisation of the shaping of the plasma core to maximise confinement and stability, whilst modifying the divertor configuration to maximise the dissipation of particles, momentum and energy. Sources of non-axisymmetic magnetic fields are available for ELM control with Resonant Magnetic Perturbations (RMPs) and correcting for intrinsic error fields (EFs), with two rows of in-vessel coils (four equally spaced toroidally above the mid-plane, eight below) and two pairs of ex-vessel coils respectively. On—and off-axis Neutral Beam Injectors (NBI) enable studies of the confinement of super Alfvénic fast ions that more closely mimics the products of fusion reactions. An extensive suite of highly resolved diagnostics is available to support a broad and deep physics programme in these key physics issues for the operation of ITER and the design of future power plants including DEMO [2] and STEP [3].

An optimal fine-alignment of the internal poloidal field coils to shape the plasma core and divertor was performed when assembling MAST-U to reduce the $n = 1$ EF source

associated with the coil design and manufacturing, which has foreseen coil shifts and tilts, of the order of mm and mrad, respectively [4]. To assess the presence of a residual $n = 1$ EF, dedicated EF identification studies have been carried out and the main results are reported in figure 2, which represents the compass scan tests executed in Ohmic scenarios with conventional divertor configurations at $I_p = 450$ kA, $B_\varphi = 0.4$ T and $I_p = 750$ kA, $B_\varphi = 0.5$ T. In both scenarios, EF identification studies suggest that a homeopathic level of correction currents are needed to minimise the intrinsic EF amplitude, of around some hundreds of A. This suggests that the intrinsic EF amplitude is smaller than in MAST, where the EF correction currents were in the kilo Ampere regime [5]. This proves that the coil alignment when assembling the device so as to minimise the intrinsic $n = 1$ EF has been a successful passive $n = 1$ EF correction strategy.

Recent results from MAST Upgrade are presented, including fast particle physics in section 2, MHD stability and maximising beta in section 3, pedestal and Edge Localised Mode (ELM) physics in section 4, plasma exhaust with an emphasis on the relative benefits of alternative divertor configurations in section 5 and plasma control and the development of high-performance plasma scenarios in section 6. A programme of extensive hardware enhancements is underway to further develop the capabilities of MAST Upgrade. These enhancements and the envisaged future MAST Upgrade programme are presented in section 7. A summary and implications of the results presented to future devices is presented in section 8.
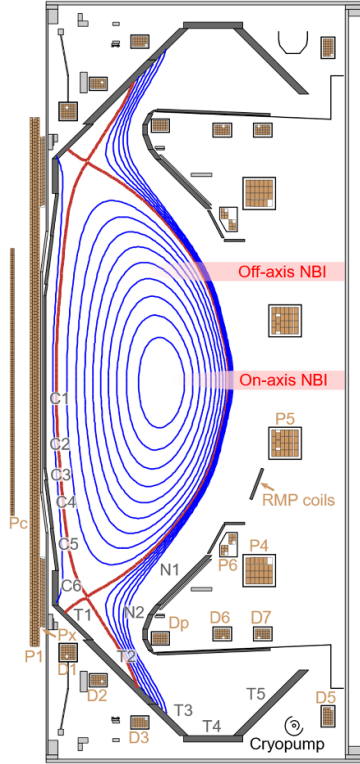
**Figure 1.** Poloidal cross-section of MAST upgrade.



**Figure 2.** Quantification of the intrinsic error field in $I_\mathrm{p} = (a)$ 450 kA and (*b*) 750 kA plasma scenarios using the compass scan technique [6].

## 2. Fast particle physics

Future large burning fusion devices with a significant $\alpha$ particle population will require good confinement of charged fusion products to maximise plasma self-heating and minimising heat fluxes arising from losses. MAST Upgrade is well suited to studying fast particle confinement and the impact of MHD instabilities, with on-and off-axis neutral beams (with tangency positions (R, Z) of (0.71 m, 0.0 m) and (0.8 m, 0.65 m) respectively) that produce anisotropic super-Alfvénic fast ions (for example, in a typical pulse the speed of the deposited fast ions $v_\mathrm{fi} \sim 2.5 \times 10^6$ m s$^{-1}$ exceeds the Alfvén speed in the core $v_\mathrm{A} \sim 1.5 \times 10^6$ m s$^{-1}$ [7]). A comprehensive suite of highly resolved diagnostics is available, including a fission chamber [8], upgraded neutron camera [7], Solid State Neutral Particle Analyser (SSNPA) [9], Fast Ion Loss Detector (FILD) [10] and a Fast-Ion Deuterium Alpha (FIDA) system [11]. Despite the closed divertors reducing the neutral density in the main chamber, inferred from mid-plane radial profiles of $n_\mathrm{e}$, $T_\mathrm{e}$ and $D_\alpha$ emission, up to 20% of the injected NBI power from both beams are lost due to charge-exchange interactions with edge neutrals [12], and including these interactions enables reconstruction of the passive FIDA signal. While this is unlikely to be an issue in future higher power devices as the main chamber neutral pressure is expected to be lower than in MAST-U, and neutrals will be more strongly attenuated by the pedestal [13], maximising the absorbed neutral beam heating power will enable MAST-U to reach more reactor-relevant conditions.
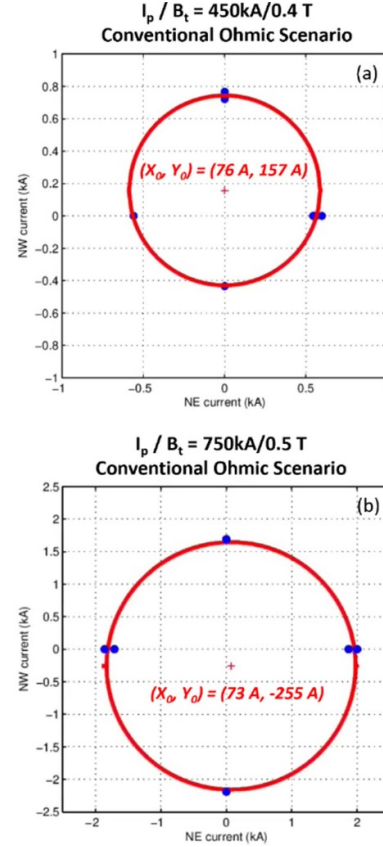
A broad spectrum of fast ion driven instabilities are excited including toroidal (TAE), compressional (CAE) and global (GAE) Alfvén eigenmodes, fishbones, as shown in figure 3, mostly due to fast ions produced by the on-axis beam. The impact of these instabilities on the thermal plasma and fast ion confinement has been studied in detail. The largest source of fast ion losses is 2/1 tearing modes that are commonly observed in NBI heated pulses (see section 3). The tearing mode amplitude typically grows throughout the NBI heated phase of a pulse that can reduce the measured neutron rate by up to 50%. Significant changes in the fast ion population are observed following sawtooth crashes [7], that can reduce the fast ion population by 40%–50% across the plasma core, in agreement with similar findings on MAST [14]. Fast ion losses in the core due to fishbones have been observed with neutron camera and FILD diagnostics, that can reduce the fast ion density by $\sim$20%, up to 35% near the magnetic axis, indicating a hollow neutron profile as the fishbone grows, then in the later phase becomes peaked in the core slightly toward the inboard side. Interpretive modelling with ASCOT [15] and FILD measurements suggest these losses are of trapped fast ions [16]. Conversely, TAEs are correlated with fast ion losses only when the off-axis neutral beam is applied, otherwise they tend to result in fast ion redistribution.

For the first time, FILD measurements indicate that CAEs and GAEs have been correlated with fast ion losses. The
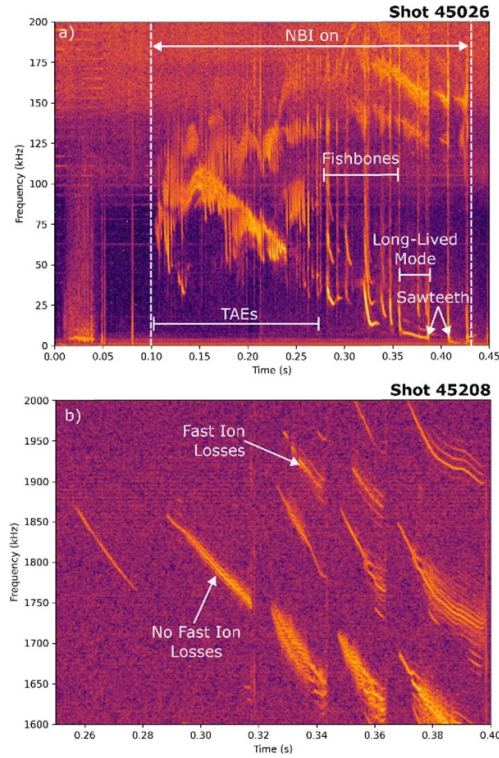
**Figure 3.** Spectrograms of magnetic fluctuations (a) illustrating commonly observed fast particle driven instabilities, including chirping/bursting TAEs, $n = 1$ internal kink modes (chirping fishbones then long-lived mode) and sawteeth (based on [17]) and (b) CAE/GAE modes and whether they correlate with fast ion losses, measured with a Fast Ion Loss Detector.



**Figure 4.** Impact of the plasma current ramp rate on the equilibrium q profile, comparing two shots with fast and slow $I_p$ ramps (top) and MSE constrained equilibrium q profiles 20 ms after the start of the $I_p$ flat-top (bottom).

location of these modes has been determined with Doppler backscattering (DBS) measurements, finding that modes that are more localised to the plasma core (up to $\sqrt{\psi_N} \sim 0.7$) result in fast ion redistribution, whereas modes localised near the edge (up to $\sqrt{\psi_N} \sim 0.9$) result in fast ion losses. Evidence for ion cyclotron emission from Ohmic plasmas has been observed in density fluctuations measured by DBS with a frequency of $\sim 3.5$ MHz [18].

Fast ion redistribution and losses due to ELMs have been measured with the FILD, SSNPA and FIDA diagnostics. Type-III ELMs are observed to have minimal impact on global fast ion confinement as the neutron rate is not strongly affected [19]. However, these ELMs result in localised fast ion losses, likely from the plasma edge, with no fast-ion acceleration correlated with ELMs. Fast ion losses due to the presence of RMPs have also been observed.

## 3. Core MHD stability and maximising beta

The avoidance of performance limiting and disruptive MHD instabilities is highly desirable to maximise fusion performance and reduce the risk of damage to the interior surfaces of a fusion device respectively. Therefore, identification and avoidance of these instabilities is a key objective of the MAST Upgrade programme. Typical plasma scenarios have a rapid
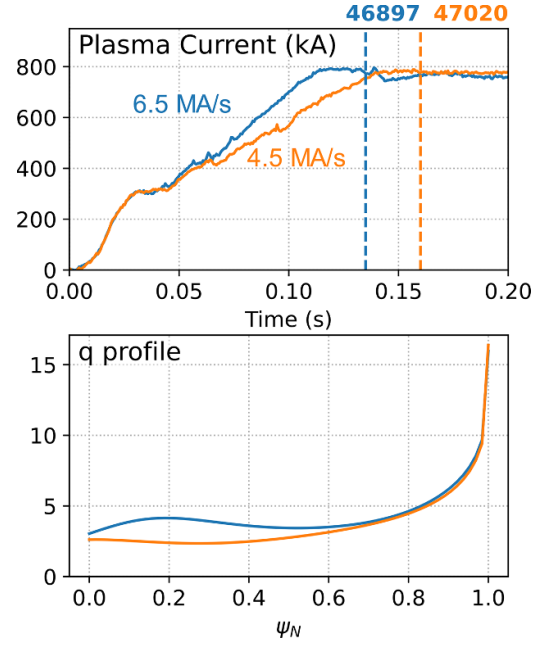
initial plasma current ramp rate, $dI_p/dt \sim 6.5$ MA s$^{-1}$, prior to the flat-top phase and Internal Reconnection Events (IREs) are common, due to the presence of a $q$ profile with reversed shear. IREs are observed to cause a transient increase in plasma current ($I_p$) and loop voltage, and reduction in plasma density, resulting in current redistribution from a hollow, reverse shear $q$ profile to a broad, monotonic one [20]. IREs have been successfully avoided with slower $I_p$ ramp rates, $\sim 3.5$–$4.5$ MA s$^{-1}$, resulting in more monotonic $q$ profiles with lower central shear, as shown in figure 4.

The performance of MAST Upgrade plasmas with strong auxiliary heating is typically moderated by $m/n = 1/1$, $2/1$ and $3/2$ modes, which dampen the rotation profile (the higher order modes mostly reduce the core rotation, whereas the lower order modes reduce the entire rotation profile) and reduce core confinement. The 1/1 mode is qualitatively similar to the long-lived mode studied on MAST [21], except that it does not always limit the pulse duration and higher order harmonics are weaker in spectrograms of magnetic field fluctuations. The 2/1 tearing mode causes a characteristic frequency of 6–10 kHz and causes flattening of the $T_e$ profile at the $q = 2$ flux surface. The rotation frequency of the mode is consistent with plasma rotation profile measurements at the $q = 2$ surface, as shown in figure 5. To avoid these instabilities, the initial $I_p$ current ramp has been optimised to avoid the IRE. The slower $I_p$ current ramp tends to reduce q$_0$ in the early $I_p$ flat-top phase, while the off-axis neutral beam provides additional current drive to help elevate $q_0$. Further plasma scenario optimisations are underway to vary $I_p$, $B_\varphi$ and elongation ($\kappa$) to maximise normalised beta ($\beta_N$), then other metrics. The off-axis neutral beam is an effective source of non-inductive current
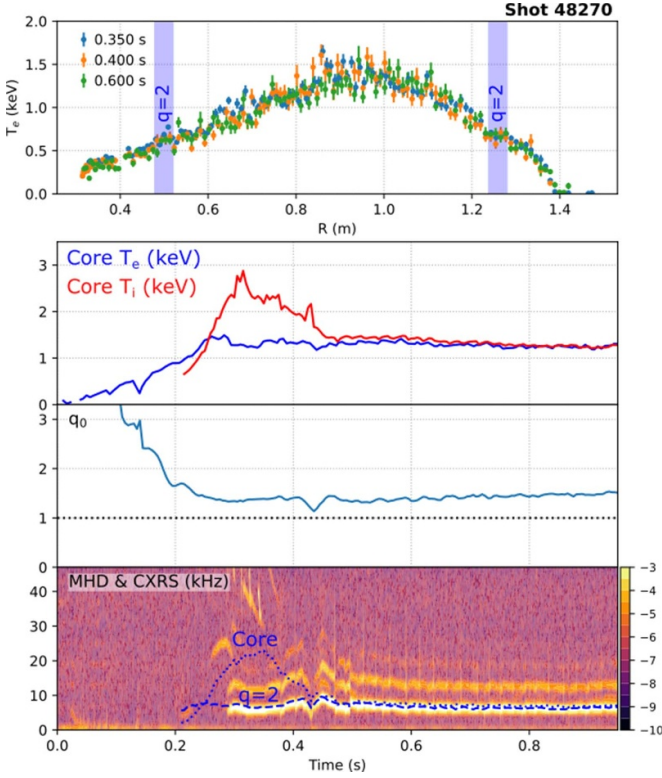
**Figure 5.** Overview of a typical pulse with a performance limiting tearing mode. Top: Thomson scattering profiles of $T_e$ showing flattening at the $q = 2$ surface, middle: core $T_e$, $T_i$, bottom: spectrogram of low frequency magnetic fluctuations with the toroidal rotation at the magnetic axis and $q = 2$ flux surface.



**Figure 6.** Electron density and temperature pedestal height in MAST [28] in double null (DN) and single null (SN) topologies and MAST upgrade.

## 4. Pedestal and ELM physics

MAST Upgrade routinely operates in the high confinement mode (H-mode), with auxiliary heating from the on- and off-axis neutral beams. Initial studies on H-mode access have concentrated on the impact of the divertor configuration on $P_{\text{L-H}}$, indicating broadly similar values for conventional and Super-X divertor configurations.

In H-mode, radial profiles of electron density ($n_e$) and temperature ($T_e$) at the edge of the confined plasma exhibit steep gradients emblematic of the edge pedestal. The density and temperature pedestal characteristics were diagnosed with a high-resolution Thomson scattering system in MAST [28] and MAST Upgrade, where the pedestal top parameters are shown in figure 6. There is significant overlap in the achieved pedestal top parameters in both devices, however MAST Upgrade is able to sustain hotter pedestals where $T_{e,\text{ped}} > 350$ eV, which was not possible in MAST with comparable auxiliary heating power. The transition from type-III to type-I ELMs is observed to occur when the power crossing the separatrix is $\sim$1.9 MW and $T_{e,\text{ped}} \sim$130 eV [29], which is lower than comparable values on MAST of $\sim$2.5 MW and 150 eV respectively [30].

The MHD and gyrokinetic stability of MAST pedestals was analysed with the ELITE and CGYRO codes [31], showing that the pedestal was constrained by kinetic ballooning and medium toroidal mode number peeling-ballooning modes. Stability analysis of MAST Upgrade pedestals [32], shown in figure 7, indicates that the higher elongation and squareness of the plasma boundary, compared with MAST, due to improved plasma shaping, enabled by the larger number of poloidal field coils and higher toroidal field in MAST Upgrade and enables operation at higher normalised pedestal pressure, closer to the peeling boundary. This analysis suggests that the squareness of the plasma boundary is close to optimal, but further improvements in pedestal stability, and in turn the pedestal pressure, are possible by increasing elongation and maximising particle pumping and auxiliary heating power available

drive that allows $q_0 > 1$ to be sustained throughout a pulse, as shown in figure 5, thus avoiding sawteeth. To date, the highest achieved $\beta_N$ is $\sim$4.2 transiently in shot 48 653, which reached a maximum stored energy of $\sim$160 kJ prior to the locking of 2/1 and 1/1 modes that resulted in a disruption. These results built on work carried out in previous campaigns where $\beta_N$ was limited to $\sim$3 by non-disruptive mode locking events [22]. In support of further optimising plasma performance, the highest achievable elongation for a given $\ell_i$ has been characterised. To date, $\kappa$ up to 2.4 has been achieved with good vertical control.

Density limits have been studied [23], finding that disruptivity increases with proximity to the Greenwald density limit [24]. Of the few density limit disruptions observed to date, they cross a threshold based on the turbulent transport for a given heating power across the separatrix [25]. Investigation of disruption causes (indicated by abnormalities in the plasma current and vertical position development) with the DECAF$^{\text{TM}}$ [26] code revealed a year-to-year (in the first and second physics campaigns) decrease by $\sim$20% of the plasma disruptivity rate. These improvements in scenario robustness were enabled through better real-time control of the plasma shape and density. Trigger instances of disruptive event chains were clustered in different parts of the operation space diagrams and plasma elongation was shown to be an important factor influencing details of the chains [27].
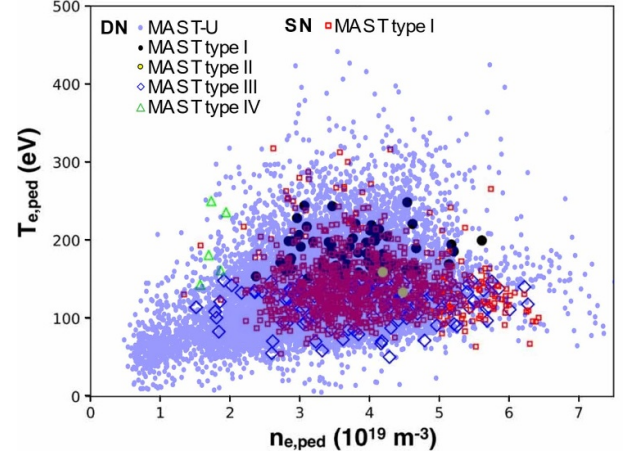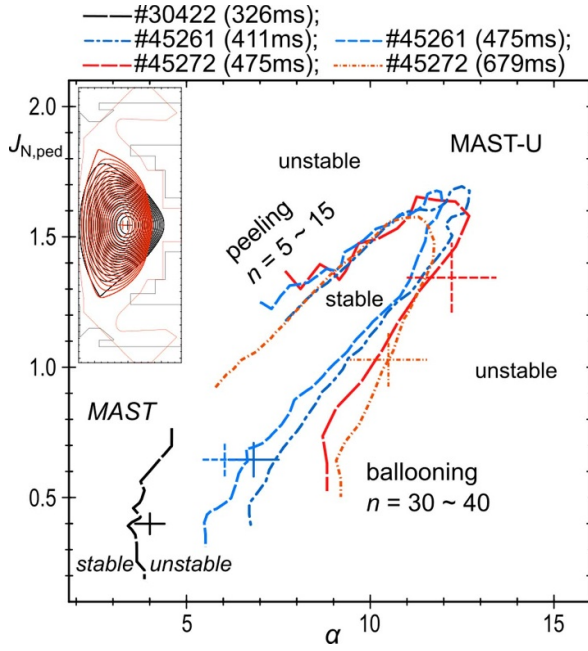
**Figure 7.** Pedestal stability boundaries in terms of normalised pedestal pressure gradient on the *x*-axis and current density on the *y*-axis on MAST (black) and MAST-U (blue, red). The inset figure shows MAST (black) and MAST-U (red) equilibria analysed.

in upcoming improvements to the device to reduce the pedestal collisionality.

Mitigation of type-I ELMs with RMPs with toroidal mode number, $n = 1$ has been achieved. The application of $n = 1$ RMPs leads to an increase in the ELM frequency and deceleration and locking of a 2/1 tearing mode that is common to typical type-I ELMy H-mode scenarios (as discussed in section 3) and then density pump-out. Removal of the RMPs results in the mode rotation accelerating and the ELM frequency decreasing to their original values.

## 5. Plasma exhaust and alternative divertor configurations

MAST Upgrade has significant flexibility to develop and study conventional and alternative divertor configurations, with and without up-down symmetry, including the X-divertor [33, 34], Super-X [35], Snowflake [36] and X-point target [37], as shown in figure 8. The early MAST Upgrade programme prioritised comparing the Super-X with a conventional divertor configuration, including the role of total flux expansion tightly baffled divertor chambers on plasma exhaust. In spherical tokamaks, the benefits of the Super-X configuration are amplified, such as higher total flux expansion ($\sim$2.5 in MAST-U, compared with $<$1.7 in TCV [38]), and consequently strong gradients in the total magnetic field from the X-point to the divertor target that is predicted to passively stabilise the movement of the detachment front [39]. Consequently, an extensive suite of diagnostics was deployed and optimised to study the Super-X divertor configuration, including 850 Langmuir probes [40], a divertor Thomson scattering system
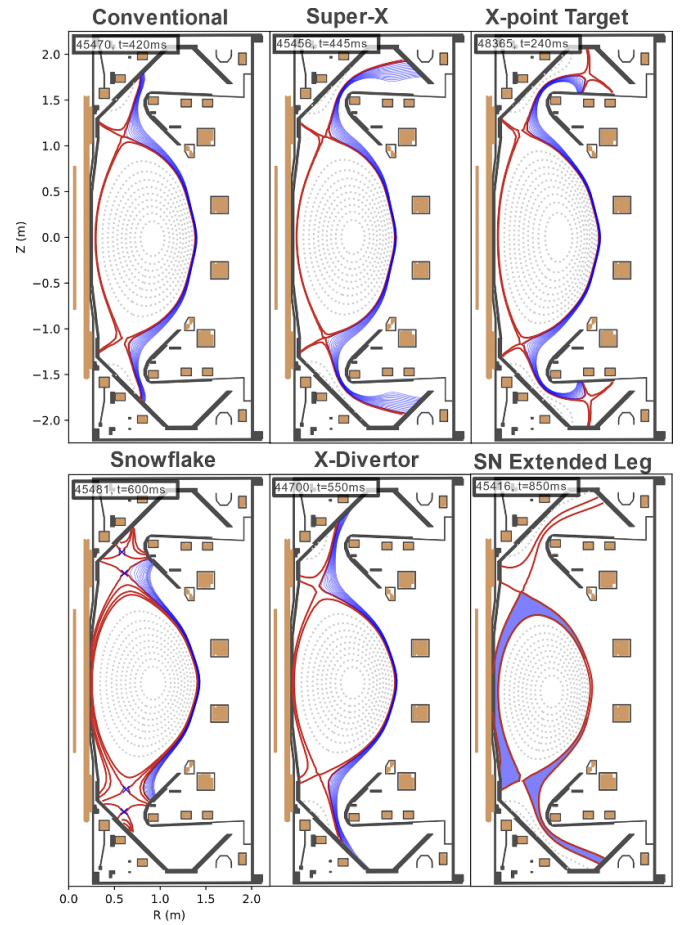


**Figure 8.** Equilibrium reconstructions of conventional and alternative divertor configurations developed on MAST-U.

[41], a multi-wavelength imaging system [42], resistive [43] and imaging [44] bolometer diagnostics, UV–visible spectrometers, neutral pressure gauges and IR thermography. Other divertor configurations are being developed and studied in parallel, particularly the snowflake [45] and X-point target.

Initial comparisons of conventional and Super-X divertor configurations were performed in Ohmic and NBI heated L-mode pulses. Experiments were performed with density ramps and repeat pulses at different (constant) flat-top density, using gas puffing to control the plasma density, to quantify the onset of divertor detachment. The detachment threshold, in terms of the estimated separatrix density, was approximately a factor of two lower in the Super-X configuration than a conventional divertor, as shown in figure 9. Detailed comparison of the detachment threshold was complicated by the onset of locked modes causing toroidal asymmetries in the divertor heat and particle flux profiles (termed 'strike point splitting' in figure 9), however the reduced detachment threshold in the Super-X configuration is in broad agreement with predictions from analytic models (e.g. [39]). The divertor surface power load was reduced by at least an order of magnitude in the Super-X configuration. The mid-plane $n_e$ and $T_e$ profiles at a given line-average density were not significantly affected by either the divertor configuration or whether the outer divertors
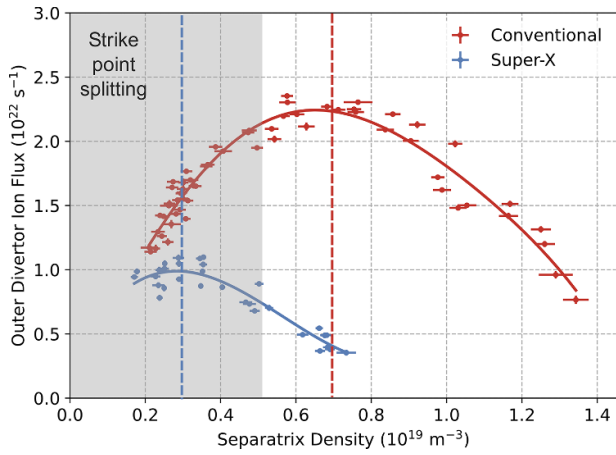
**Figure 9.** Measured total divertor ion flux in conventional (red) and Super-X (blue) divertor configurations. Estimated detachment thresholds are given by vertical dashed lines.



**Figure 10.** Profiles of the electron temperature (red) and power losses due to plasma-atom interactions (blue) along the separatrix flux surface from the divertor entrance to the target in conventional and Super-X divertor configurations simulated with SOLPS-ITER.

were detached. This detachment behaviour in the Super-X divertor configuration is well reproduced in predictive [46] and interpretive SOLPS-ITER simulations [47], however the simulations of the conventional configuration do not exhibit the characteristic roll-over in the total divertor ion flux, which is thought to be due to a reduction in the upstream separatrix pressure in experiments from strong power losses originating from the strong gas fuelling applied to reach the required core line-average density. Characterisation of detachment onset in other alternative divertor configurations is underway.

Multi-wavelength imaging of the $D_2$ Fulcher band emission from the lower divertor chamber was used to estimate the position of the ionisation front, where the dominant form of plasma-neutral interactions transitions from electron impact ionisation to plasma-molecule interactions [48]. As the plasma conditions in the divertor chambers trend toward deeper detachment, the ionisation front moves from the outer strike point towards the divertor entrance. The observed sensitivity of the ionisation front movement with increasing midplane separatrix density agrees well with interpretive SOLPS-ITER simulations [49]. There is a clear reduction in the sensitivity of the front position to changes in the separatrix density as the emission front moves through regions exhibiting strong gradients in the total magnetic field, in agreement with analytic models [39, 50].

Studies of NBI heated L-mode pulses with conventional, Super-X and an intermediate, elongated, divertor configuration elucidate the benefits of increased divertor volume on power and particle exhaust [51]. In the elongated and Super-X divertor configurations after the onset of detachment, the ionisation region in the divertor chamber extends to a fixed major radius, insensitive to increases in the major radius of the outer strike points. Downstream of the ionisation region, any additional divertor volume afforded by a larger outer strike point major radius increases ion sinks, including Molecular Activated Recombination (MAR) and Electron-Ion Recombination (EIR), and power losses due to plasma-neutral
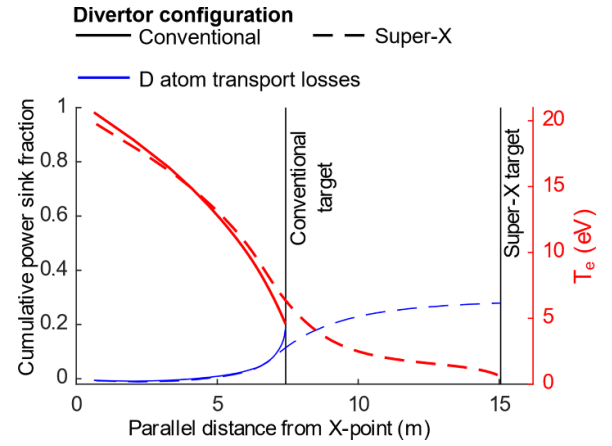
interactions that reduce divertor target power and particle fluxes.

Experiments performed in type-I ELMy H-mode scenarios with conventional and Super-X divertor configurations and similar core shaping are in broad agreement with the L-mode studies, in terms of ease of access to divertor detachment in the Super-X configuration and effective decoupling of the mid-plane pedestal profiles and the divertor configuration and detachment state. In 750 kA scenarios, which maximise the ratio of the separatrix density at the midplane and the parallel heat flux entering the divertor chambers to ease access to attached divertor conditions, with ~3 MW of NBI heating power, the conventional divertor configuration was attached and the Super-X detached. In common with L-mode experiments, global confinement parameters, including $H_{IPB98y,2}$ and $\beta$, and core and pedestal $n_e$ and $T_e$ profiles were also unaffected by whether the divertor was in a conventional or Super-X configuration and whether the outer divertors are attached or detached. These observations are in good qualitative agreement with SOLPS-ITER simulations, shown in figure 10, that the plasma conditions in conventional and Super-X configurations are similar for otherwise similar boundary conditions, but $T_e$ at the divertor entrance is lower in the Super-X configuration due to higher power losses due to plasma-neutral interactions in the additional divertor volume where $T_e < 5$ eV. The divertor neutral compression, the ratio of the lower divertor and main chamber neutral pressures, is typically 100–300, with the Super-X having higher compression despite the outer divertors being detached.

The fundamental mechanisms governing detachment in the Super-X divertor configuration have been studied in experiments via spectroscopic measurements interpreted using a sophisticated Bayesian framework BaSPMI [48]. To correctly interpret these measurements, it is necessary to account for plasma-molecule interactions and measurements of the $D_2$ Fulcher band emission profile are needed to discern between emission due to electron impact excitation, which in turn can be used to estimate where ionisation of neutrals occurs, and
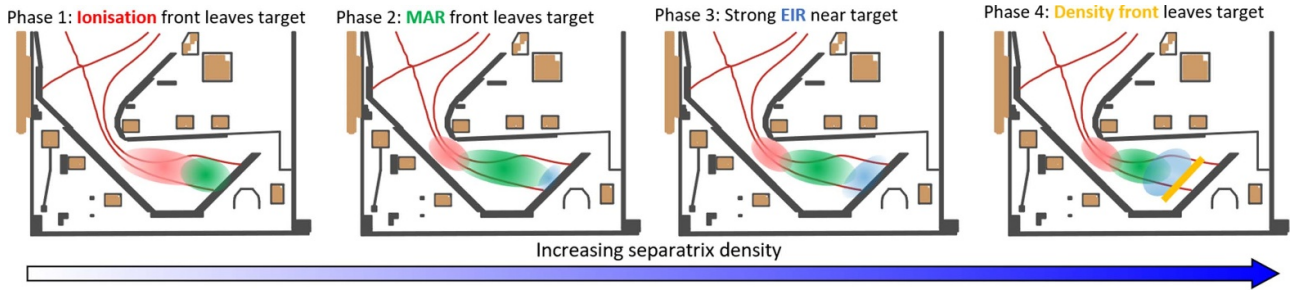
**Figure 11.** Phases of divertor detachment observed in spectroscopic studies of the lower divertor chamber.

plasma-molecule interactions. In Ohmic and NBI heated L-mode pulses, 4 distinct detachment phases were observed, as shown in figure 11. At detachment onset, in phase 1, the ionisation front, inferred from the trailing edge of $D_2$ Fulcher band emission, pulls away from the divertor target, with evidence of MAR occurring downstream. In phase 2, the region where MAR interactions occur pulls away from the target and the outer divertor particle flux reduces with increasing fuelling, there is evidence of EIR occurring downstream, suggestive that the target electron temperature $T_{e,t} \sim 0.8$ eV. In phase 3, the frequency of EIR interactions increases and $T_{e,t} \sim 0.5$ eV. In phase 4, normally prior to a density limit disruption, all three emission regions move toward the divertor entrance and the peak in the divertor electron density pulls away from the target and $T_{e,t} \ll 0.5$ eV. Due to $T_e$ being low across the outer divertor leg in the Super-X configuration, radiation from carbon is thought to have a negligible contribution to power dissipation in the divertor chambers. Moreover, the low temperature in the divertor results explains why EIR in the divertor is prevalent, despite the density being modest ($\sim 1$–$3 \times 10^{19}$ m$^{-3}$) and SOLPS-ITER simulations being more susceptible to inaccuracies in the rates of atomic and molecular processes, in particular of molecular charge-exchange [52, 53]. Radiation trapping from deuterium and carbon are predicted to be small, based on predictive simulations with the CRETIN code [54].

## 6. Plasma control and development of high-performance scenarios

The MAST Upgrade Plasma Control System (PCS) is based on the framework developed at General Atomics [55] with improvements to accommodate the larger number of gas injection locations and coil current control to independently control Ohmic heating (via either loop voltage or plasma current), shape and position of the plasma boundary and the outer divertor legs [56]. Real-time sensing of the inner and outer radii of the Last Closed Flux Surface (LCFS) at the mid-plane, radial and vertical position of the lower X-point and the position of the lower outer divertor strike point is provided by LEMUR [57], a local higher order expansion of poloidal flux, fitted to magnetic field and flux measurements and constrained by the Grad-Shafranov equation in the vacuum region. Prior to deployment on MAST-U, LEMUR was successfully validated against experiments on DIII-D

[58]. Real-time manipulation of the plasma shape parameters sensed by LEMUR, and feedforward control of other parameters (e.g. squareness of the LCFS, poloidal flux expansion at the outer divertor, etc) independently is facilitated by linear shape control 'virtual circuits' that map changes to individual plasma shape parameters, whilst keeping the others of interest fixed, to changes in poloidal field coil currents [59]. Control of the plasma density is facilitated by real-time measurements of the line-integrated density using an interferometer chord at the mid-plane [60] and an arbitrary combination of gas valves. Detachment control has been successfully demonstrated using multi-wavelength imaging to estimate the position of the ionisation front in the lower divertor chamber, as discussed in section 5, and gas fuelling from the main chamber was used to vary the detachment state.

Plasma scenarios have been developed at $I_p = 450$, 600, 750, 1000 kA, mostly with either conventional or Super-X divertor configurations. Plasma breakdown is performed via direct induction, where the toroidal electric field is induced via the central solenoid and thermionic emission of electrons from a hot filament provides a source of free electrons [29]. The initial loop voltage and pre-fill gas pressure have been optimised to minimise solenoid flux consumption and is robust to changes in vessel conditions, such as after boronisations. In the $I_p$ ramp-up phase, the plasma volume, outer radius and elongation expand rapidly to slow current penetration to the magnetic axis, thus maximising $q_0$ and minimising $\ell_i$. This is favourable for sustaining strong shaping of the plasma boundary, in particular high elongation, and to avoid the onset of low order performance-limiting instabilities such as the long-lived mode [21], but would increase the likelihood of reverse magnetic shear which is destabilising for helical core type modes.

The development of high-performance scenarios has two elements, concentrating on increasing $I_p$, to increase confinement of the thermal and fast particle populations and maximising $\beta$ at intermediate $I_p$, as discussed in section 3. The 750 kA scenarios are the most widely used to date, benefitting from satisfactory confinement for the majority of the scientific programme and can be executed with Ohmic heating only or with NBI with sufficiently long $I_p$ flat-top duration. Therefore, these scenarios are the most mature and thoroughly studied. To develop a robust H-mode scenario, the gap between the inner wall and the LCFS is at least 3 cm, the vertical position is optimised to maintain a connected double null topology and only fuelling from the high-field side is used, all
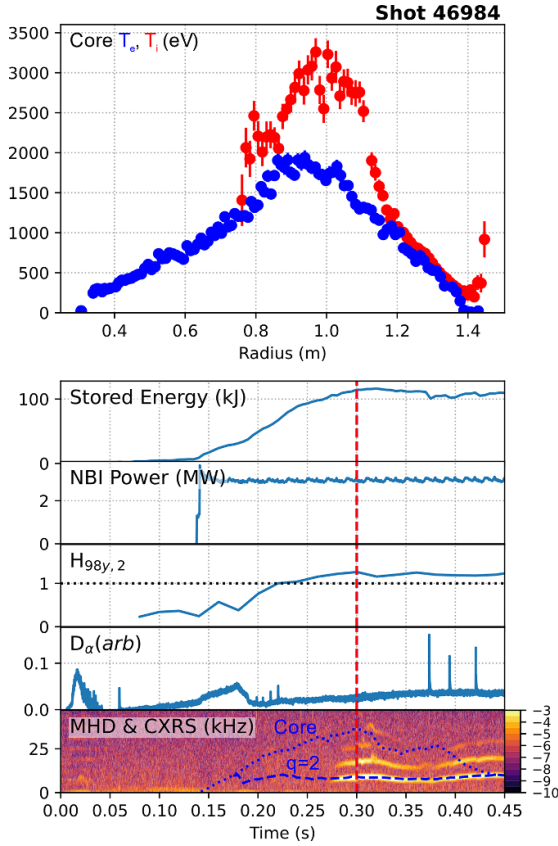
**Figure 12.** Top—ion and electron temperature profiles in a high confinement shot. Below—time traces of plasma stored energy, injected NBI power, normalised energy confinement time, main chamber $D\alpha$ emission and MHD activity with bulk plasma rotation data overlaid.

of which promote H-mode access. With these optimisations applied, maximum core electron and ion temperatures of 2 keV and 3 keV respectively with energy confinement normalised to the ITER scaling [61] $H_{\mathrm{IPB98y,2}} \sim 1.3$ have been achieved, as shown in figure 12. As discussed in section 3, the performance of these scenarios is typically limited by 2/1 tearing modes, which tends to reduce the energy confinement to $H_{\mathrm{IPB98y,2}} \sim 1$. The mode amplitude is moderated, and its rotation frequency maintained, via a combination of off-axis neutral beam injection, moderate gas fuelling after the L-H transition and reducing $\beta$ and $\kappa$ [29].

The development of higher $I_{\mathrm{p}}$ scenarios is underway and exhibits similar performance limiting MHD and shares common amelioration strategies with the 750 kA scenarios. To date, a 1000 kA scenario with a conventional divertor has reached 500 ms duration. Further optimisations of this scenario, through careful tailoring of gas fuelling, elongation, timings of NBI injection and toroidal field are expected to improve scenario performance and pulse duration further.

## 7. Hardware enhancements and future programme

A phased programme of enhancements to the heating, fuelling and pumping capabilities of MAST Upgrade are underway

to access more reactor-relevant plasma conditions, including lower collisionality in the core, pedestal and divertor, higher divertor heat flux, maximum divertor neutral pressure and higher beta for longer pulses. In 2024, a divertor cryopump will be operational to provide a tenfold increase in particle pumping to significantly improve particle control for longer pulse operations and is predicted to expand the range of operating parameters where attached divertor operation is possible [62]. In 2025, a 1.6 MW electron Bernstein wave heating and current drive system with injection frequencies of 28 GHz and 34.8 GHz will enable studies of on-and off-axis heating and current drive in the plasma current ramp-up and flat-top phases. Also in 2025, two additional NBIs will be installed, increasing the maximum injected power by up to 2.5 MW of off-axis heating and 2.5 MW intermediate between the on-axis and off-axis injectors, to double the total neutral beam heating power to a maximum of 10 MW and to further tailor the fast ion pressure profile for the avoidance of energetic particle modes. In parallel, a high frequency pellet injector will be commissioned to study the impact of reactor-relevant fuelling on scenario performance and control, emphasising studies to optimise core and pedestal confinement with acceptable power exhaust in the presence of transient particle fluxes.

These new capabilities will significantly broaden the operational space of MAST Upgrade and facilitate deep physics studies into key physics issues for future tokamaks, including non-inductive current drive with electron Bernstein waves, fast particle physics with fine control of the fast ion pressure profile, studies of core and pedestal confinement and MHD stability at higher performance and their integration with highly dissipative alternative divertor configurations. Future physics programmes will aim to advance understanding in these areas in parallel as the capabilities of the device improves. For example, additional heating power and current drive, both on-and off-axis, are expected to facilitate sustainment of higher $q_0$ due to additional off-axis current drive, to study confinement and stability with more STEP-relevant q profiles [63] with $q_0 \sim 2$.

It is envisaged that studies of power and particle exhaust will advance to study detachment induced via impurity seeding and understanding the controllability of divertor detachment in a wider variety of divertor configurations, including the X-point target, X divertor and snowflake and their response to transients arising from pellet injection and MHD, including ELMs. At higher heating power and higher core plasma pressure, and consequently higher Shafranov shift, may alter the balance of heat and particle fluxes between the inner and outer divertors in a double-null topology that can inform the development of exhaust solutions for future devices such as STEP.

The development and study of stationary high-performance regimes will have greater emphasis in future campaigns, as the lower pedestal collisionality afforded by the higher heating power and pumping speed is expected to facilitate access to naturally ELM-free pedestal regimes such as the QH-mode as well as ELM control with RMPs. The integration of stationary ELM-free pedestals with detached divertors, which is required in ITER [64], DEMO [65] and other future devices will be studied, building on these promising initial results. In

parallel, the programme of experiments will be accompanied by modelling predictions to test predictive tools and deepen our understanding of experiments.

## 8. Summary and implications for future devices

Recent results from MAST Upgrade have advanced our understanding in key physics areas that concern the design and operation of future fusion devices.

Fast particle physics studies have found that the largest source of fast ion losses is $m/n = 2/1$ tearing modes that are commonly observed in NBI heated pulses, which can reduce the measured neutron rate by up to 50%. Sawtooth crashes can also reduce the fast ion population by 40%–50% across the plasma core. A rich spectrum of fast ion driven instabilities has been observed, including fishbones (which can reduce the fast ion density by up to 35% near the magnetic axis). TAEs have been observed to correlate with fast ion losses only when off-axis neutral beam injection is applied, otherwise they lead to fast ion redistribution. For the first time, fast ion losses correlated with CAEs and GAEs have been observed, with more core-localised modes (up to $\sqrt{\psi_N} \sim 0.7$) resulting in fast ion redistribution, whereas more edge-localised modes (up to $\sqrt{\psi_N} \sim 0.9$) result in fast ion losses. These observations provide strongest tests for predictive models used to estimate the impact of bulk plasma and fast ion driven MHD ion energetic particle confinement in current and future devices.

MHD stability studies have concentrated on maximising beta and the avoidance of performance-limiting instabilities. Optimisation of the $I_p$ ramp-up phase has been performed to avoid reverse-shear $q$ profiles that occur at high $dI_p/dt$ that cause IREs. The presence of $m/n = 1/1$, $2/1$ and $3/2$ modes moderates the achievable performance through damping toroidal rotation in the plasma core and reducing energy confinement. Off-axis neutral beam injection allows for sustainment of $q0 > 1$, avoiding sawteeth. To date, $\beta_N \sim 4.2$ has been achieved transiently, and improvements in the highest achievable $\beta$ and energy confinement time have been observed at higher elongation, $\kappa$, reaching values of 2.4. Increasing $\kappa$ further in future campaigns, is expected to yield further improvements in plasma performance, and facilitates studies of plasma stability in strongly shaped plasmas towards STEP-relevant values of $\sim 2.8$ [63]. Observations of the density limit are consistent with crossing a threshold based on brubulent transport across the separatrix, however in general it was observed that the plasma disruptivity rate reduced by $\sim 20\%$ through improvements in real-time control of the plasma shape and density.

In studies of pedestal and ELM physics, the electron temperature at the pedestal top could exceed 350 eV, higher than in MAST, which had similar levels of auxiliary heating power. MHD and gyrokinetic stability analysis suggests that improved plasma shaping, in particular higher elongation and squareness of the confined plasma, are responsible. This analysis suggests that further improvements in pedestal stability are possible by further increasing elongation. In future

campaigns, higher auxiliary heating power and particle pumping will be available to study hotter, less collisional pedestals towards stationary ELM-free regimes that are required in future devices. Mitigation of type-I ELMs with $n = 1$ RMPs has been observed, as well as rotation breaking of a 2/1 tearing mode and density pump-out when RMPs are applied. This is a first step towards the development of ELM control with RMPs that is needed in ITER and could be required in other future devices.

Experiments studying plasma exhaust have elucidated benefits of the Super-X divertor configuration and deepened understanding of divertor detachment. In Ohmic and NBI heated L-mode experiments, it was found that the separatrix density at the mid-plane required to detach the outer divertors is approximately 50% lower in the Super-X configuration compared with a conventional divertor, in agreement with SOLPS-ITER and analytic models, while the mid-plane $n_e$ and $T_e$ profiles were unaffected. In H-mode experiments optimised to maximise the heat flux to the outer divertors, they were found to be attached in the conventional and detached in the Super-X configurations with no noticeable impact on the edge pedestal profiles or global energy confinement. These initial results provide fresh insights into the benefits of alternative divertor configurations that are being considered for DEMO [66] and STEP [63]. The mechanisms governing detachment have been studied via spectroscopic measurements, elucidating the key role of plasma-molecule interactions, including the presence of MAR at the onset of detachment. At deeper levels of detachment, the location where MAR occurs moves from the divertor target towards the divertor entrance, with EIR occurring close to the divertor target. Simulations of these experiments are susceptible to inaccuracies in the rates of atomic and molecular processes, in particular molecular charge-exchange, that have motivated improvements in these data. In turn, these improvements should improve the accuracy of predictions of plasma exhaust in future devices.

Advances in the development and study of high-performance plasmas and alternative divertor configurations have been enabled by real-time sensing and control of the shape of the confined plasma and outer divertor legs, as well as real-time density control. Scenarios with plasma currents spanning 450 kA to 1000 kA have been developed, mostly with conventional and Super-X divertor configurations. Good energy confinement has been achieved, reaching maximum electron and ion temperatures of 2 keV and 3 keV respectively, and corresponding normalised energy confinement time $H_{\mathrm{IPB98y,2}} \sim 1.3$.

An extensive programme of enhancements further expand the operational space of MAST Upgrade towards more reactor-relevant conditions. In 2024, divertor cryopumping will be available to significantly improve particle control for longer pulses and to facilitate access to attached divertor conditions to study detachment onset and control. Subsequently, the neutral beam heating power will be doubled from 5 MW to 10 MW to reach higher $\beta$, lower collisionality to study energy confinement, prioritising the presence and impact of electromagnetic modes on electron energy confinement [67, 68]. A

1.6 MW electron Bernstein wave heating and current drive system will be a substantial source of additional electron heating that will enable studies of mode conversion physics and on- and off-axis current drive efficiency in support of STEP. A new high frequency pellet injector will be commissioned to provide reactor-relevant fuelling and enable studies of its impact on the core, pedestal and divertor.

## Acknowledgments

## ORCID iDs

J.R. Harrison https://orcid.org/0000-0003-2906-5097
S. Ahmed https://orcid.org/0000-0002-7732-5765
H. Anand https://orcid.org/0000-0002-9632-5680
Y. Andrew https://orcid.org/0000-0003-0094-3503
L.C. Appel https://orcid.org/0000-0001-9259-6240
M. Barnes https://orcid.org/0000-0002-0177-1689
J. Berkery https://orcid.org/0000-0002-8062-3210
M. Bernert https://orcid.org/0000-0003-1131-0867
W. Boeglin https://orcid.org/0000-0001-9932-9161
C. Bowman https://orcid.org/0000-0002-0813-2206
J. Bradley https://orcid.org/0000-0002-8833-0180
D. Brida https://orcid.org/0000-0002-8647-7058
P.K. Browning https://orcid.org/0000-0002-7089-5562
D. Brunetti https://orcid.org/0000-0001-8650-3271
J. Buchanan https://orcid.org/0000-0001-8650-3271
M. Cecconello https://orcid.org/0000-0002-2571-1920
J. Clark https://orcid.org/0000-0002-2571-1920
C. Cowley https://orcid.org/0000-0001-7065-8922
N. Crocker https://orcid.org/0000-0003-2379-5814
I. Cziegler https://orcid.org/0000-0003-1040-8918
G.L. Derks https://orcid.org/0000-0003-3420-0388
R. Doyle https://orcid.org/0000-0002-4771-4081
M. Dreval https://orcid.org/0000-0003-0482-0981
M. Dunne https://orcid.org/0000-0002-5259-9970
B.P. Duval https://orcid.org/0000-0001-7783-129X
M. Faitsch https://orcid.org/0000-0002-9809-7490
F. Federici https://orcid.org/0000-0002-9354-7309
N. Fedorczak https://orcid.org/0000-0001-7123-7433
F. Felici https://orcid.org/0000-0001-7585-376X
A.R. Field https://orcid.org/0000-0003-0671-9668
R. Fitzpatrick https://orcid.org/0000-0003-0671-9668
L. Frassinetti https://orcid.org/0000-0002-9546-4494
D. Gahle https://orcid.org/0000-0002-4434-7626
J. Galdon-Quiroga https://orcid.org/0000-0002-7415-1894
L. Garzotti https://orcid.org/0000-0002-3796-9814
T. Gheorghiu https://orcid.org/0000-0003-4254-9790
S. Gibson https://orcid.org/0000-0003-3754-6130
K.J. Gibson https://orcid.org/0000-0001-9321-5091
V.H. Hall-Chen https://orcid.org/0000-0001-6009-3649
C.J. Ham https://orcid.org/0000-0001-9190-8310
S.S. Henderson https://orcid.org/0000-0002-8886-1256
C. Hickling https://orcid.org/0000-0003-0348-6926
B. Hnat https://orcid.org/0000-0001-6498-2953
L. Howlett https://orcid.org/0000-0001-8105-8180
J. Hughes https://orcid.org/0000-0003-4802-4944
K. Imada https://orcid.org/0000-0002-8128-2438
P. Jacquet https://orcid.org/0000-0001-7919-1206
Y.O. Kazakov https://orcid.org/0000-0001-6316-5441
D. King https://orcid.org/0000-0001-5128-5083
M. Knolker https://orcid.org/0000-0002-8468-8767
B. Kool https://orcid.org/0000-0002-1636-7400
M. Kotschenreuther https://orcid.org/0000-0001-6327-877X
A.W. Leonard https://orcid.org/0000-0001-9356-1074
B. Lipschultz https://orcid.org/0000-0001-5968-3684
Y.Q. Liu https://orcid.org/0000-0002-8192-8411
B.A. Lomanowski https://orcid.org/0000-0003-2226-2004
N. Lonigro https://orcid.org/0000-0001-8581-0384
J. Lore https://orcid.org/0000-0002-9192-465X
J. Lovell https://orcid.org/0000-0001-9565-3466
S. Mazzi https://orcid.org/0000-0001-6491-8759
G. McArdle https://orcid.org/0000-0003-0888-0105
K.G. McClements https://orcid.org/0000-0002-5162-509X
K. McKay https://orcid.org/0000-0003-1822-7994
A. McLean https://orcid.org/0000-0002-0697-4397
B.F. McMillan https://orcid.org/0000-0003-1509-2940
C.A. Michael https://orcid.org/0000-0003-1804-870X
F. Militello https://orcid.org/0000-0002-8034-4756
D. Morbey https://orcid.org/0000-0001-6207-9832
D. Moulton https://orcid.org/0009-0001-8439-9551
O. Myatra https://orcid.org/0000-0002-1469-2429
A.O. Nelson https://orcid.org/0000-0002-9612-1936
M.G. O'Mullane https://orcid.org/0000-0002-2160-4546
H.J.C. Oliver https://orcid.org/0000-0002-7302-085X
P. Ollus https://orcid.org/0000-0003-2558-1457
T. Osborne https://orcid.org/0000-0003-2641-4597
N. Osborne https://orcid.org/0000-0002-6079-9550
B.S. Patel https://orcid.org/0000-0003-0121-1187
C. Paz-Soldan https://orcid.org/0000-0001-5069-4934
L. Piron https://orcid.org/0000-0002-7928-4661
C. Piron https://orcid.org/0000-0002-4441-9781
H. Reimerdes https://orcid.org/0000-0002-9726-1519
T. Rhodes https://orcid.org/0000-0002-8311-4892
J.F. Rivero-Rodriguez https://orcid.org/0000-0001-5074-0267
C.M. Roach https://orcid.org/0000-0001-5856-0287
K. Ronald https://orcid.org/0000-0002-8585-0746
P. Ryan https://orcid.org/0000-0002-7133-6156

D. Ryan ⓘ https://orcid.org/0000-0002-7735-3598
S. Saarelma ⓘ https://orcid.org/0000-0002-6838-2194
S. Sabbagh ⓘ https://orcid.org/0000-0003-1077-8118
O. Sauter ⓘ https://orcid.org/0000-0002-0099-6675
P. Shi ⓘ https://orcid.org/0000-0002-1853-0726
V. A. Soukhanovskii ⓘ https://orcid.org/0000-0001-5519-0145
D. Speirs ⓘ https://orcid.org/0000-0001-5705-6126
G. Staebler ⓘ https://orcid.org/0000-0002-1944-1733
C. Theiler ⓘ https://orcid.org/0000-0003-3926-1374
M. Tobin ⓘ https://orcid.org/0000-0003-2276-6448
M. Vallar ⓘ https://orcid.org/0000-0002-1792-6702
R.G.L. Vann ⓘ https://orcid.org/0000-0002-3105-2546
K. Verhaegh ⓘ https://orcid.org/0000-0002-0500-2764
C. Vincent ⓘ https://orcid.org/0000-0002-7227-409X
S. Wiesen ⓘ https://orcid.org/0000-0002-3696-5475
T.A. Wijkamp ⓘ https://orcid.org/0000-0003-3110-8682
H.R. Wilson ⓘ https://orcid.org/0000-0003-3333-7470
V. Zamkovska ⓘ https://orcid.org/0000-0001-8437-4576

## References

[1] Menard J.E. *et al* 2017 *Nucl. Fusion* **57** 102006
[2] Federici G. *et al* 2019 *Nucl. Fusion* **59** 066013
[3] Wilson H.R. *et al* 2020 *Commercialising Fusion Energy* (IOP Publishing) p 81
[4] Piron L., Kirk A., Liu Y.Q., Cunningham G., Carr M., Gowland R., Katramados I. and Martin R. 2020 *Fusion Eng. Des.* **161** 111932
[5] Kirk A., Liu Y., Martin R., Cunningham G. and Howell D. 2014 *Plasma Phys. Control. Fusion* **56** 104003
[6] Hender T.C. *et al* 1992 *Nucl. Fusion* **32** 2091
[7] Cecconello M. *et al* 2023 *Plasma Phys. Control. Fusion* **65** 035013
[8] Vincent C., Allan S., Naylor G., Stephen R., Bray S., Thornton A. and Kirk A. 2022 *Rev. Sci. Instrum.* **93** 093509
[9] Prechel G., Fil N., Liu D., Heidbrink W.W., Michael C. and Jackson A.R. 2022 *Rev. Sci. Instrum.* **93** 113517
[10] Rivero-Rodriguez J.F. *et al* 2018 *Rev. Sci. Instrum.* **89** 10I112
[11] Michael C.A. *et al* 2013 *Plasma Phys. Control. Fusion* **55** 095007
[12] Ollus P. *et al* 2024 *Plasma Phys. Control. Fusion* **66** 025009
[13] Mordijck S. 2020 *Nucl. Fusion* **60** 082006
[14] Cecconello M. and Sperduti A. 2018 *Plasma Phys. Control. Fusion* **60** 055008
[15] Hirvijoki E., Brizard A., Snicker A. and Kurki-Suonio T. 2013 *Phys. Plasmas* **20** 092505
[16] Rivero-Rodriguez J.F. *et al* 2023 *5th European Conf. on Plasma Diagnostics* (*Crete, Greece*, *23 April 2023*) (available at: https://ecpd2023.eventsadmin.com/Home/Welcome)
[17] Jackson A. 2023 *49th European Physical Society Conf. on Plasma Physics* (*Bordeaux, France*, *3–7 July 2023*) (available at: https://lac913.epfl.ch/epsppd3/2023/html/Mo/Mo_MCF92_McClements.pdf)
[18] Rhodes T.L. *et al* 2022 *Rev. Sci. Instrum.* **93** 113549
[19] Velarde L. *et al* 2023 *49th European Physical Society Conf. on Plasma Physics* (*Bordeaux, France*, *3–7 July 2023*) (available at: https://lac913.epfl.ch/epsppd3/2023/html/contrib.html)
[20] Gibson S. *et al* 2023 *49th European Physical Society Conf. on Plasma Physics* (*Bordeaux, France*, *3–7 July 2023*) (available at: https://lac913.epfl.ch/epsppd3/2023/html/TitleComments.html)
[21] Chapman I.T., Hua M.-D., Pinches S.D., Akers R.J., Field A.R., Graves J.P., Hastie R.J. and Michael C.A. 2010 *Nucl. Fusion* **50** 045007
[22] Berkery J.W., Sabbagh S.A., Kogan L., Gibson S., Ryan D., Zamkovska V., Butt J., Harrison J. and Henderson S. 2023 *Plasma Phys. Control. Fusion* **65** 045001
[23] Berkery J.W. *et al* 2023 *Plasma Phys. Control. Fusion* **65** 095003
[24] Greenwald M., Terry J.L., Wolfe S.M., Ejima S., Bell M.G., Kaye S.M. and Neilson G.H. 1988 *Nucl. Fusion* **28** 2199
[25] Giacomin M., Pau A., Ricci P., Sauter O. and Eich T. (the ASDEX Upgrade Team, JET Contributors and the TCV Team) 2022 *Phys. Rev. Lett.* **128** 185003
[26] Sabbagh S.A. *et al* 2023 *Phys. Plasmas* **30** 111945
[27] Sabbagh S. *et al* 2023 High accuracy, multi-device physics-based tokamak disruption prediction and forecasting with first real-time demonstration *2023 IAEA Fusion Energy Conf.* (*London*, *16–21 October 2023* ) p 2038 (available at: https://www.iaea.org/events/fec2023)
[28] Smith S.F., Kirk A., Chapman-Oplopoiou B., Clark J.G., Ham C.J., Horvath L., Maggi C.F., Scannell R. and Saarelma S. 2022 *Plasma Phys. Control. Fusion* **64** 045024
[29] Thornton A.J. *et al* 2023 Development of integrated plasma scenarios in MAST-U *2023 IAEA Fusion Energy Conf.* (*London*, *16–21 October 2023*) (available at: https://www.iaea.org/events/fec2023 )
[30] Kirk A., O'Gorman T., Saarelma S., Scannell R. and Wilson H.R. 2009 *Plasma Phys. Control. Fusion* **51** 065016
[31] Knolker M., Osborne T., Belli E., Henderson S., Kirk A., Kogan L., Saarelma S. and Snyder P.B. 2021 *Nucl. Fusion* **61** 046041
[32] Imada K. *et al* 2024 *Nucl. Fusion* **64** 086002
[33] Takase H. 2001 *J. Phys. Soc. Japan* **70** 609
[34] Kotschenreuther M., Valanju P.M., Mahajan S.M. and Wiley J.C. 2007 *Phys. Plasmas* **14** 072502
[35] Valanju P.M., Kotschenreuther M., Mahajan S.M. and Canik J. 2009 *Phys. Plasmas* **16** 056110
[36] Ryutov D. 2007 *Phys. Plasmas* **14** 064502
[37] LaBombard B. *et al* 2015 *Nucl. Fusion* **55** 053020
[38] Theiler C. *et al* 2017 *Nucl. Fusion* **57** 072008
[39] Lipschultz B., Parra F.I. and Hutchinson I.H. 2016 *Nucl. Fusion* **56** 056007
[40] Ryan P., Elmore S.D., Harrison J.R., Lovell J. and Stephen R. 2023 *Rev. Sci. Instrum.* **94** 103501
[41] Clark J.G., Bowden M.D., Kim Y., Parry B., Rose E., Sarwar R. and Scannell R. 2022 *Rev. Sci. Instrum.* **93** 103534
[42] Feng X. *et al* 2021 *Rev. Sci. Instrum.* **92** 063510
[43] Lovell J., Reinke M.L., Field A.R. and Lomanowski B.A. 2023 *Rev. Sci. Instrum.* **94** 023509
[44] Federici F., Reinke M.L., Lipschultz B., Thornton A.J., Harrison J.R., Lovell J.J. and Bernert M. 2023 *Rev. Sci. Instrum.* **94** 033502
[45] Soukhanovskii V.A., Cunningham G., Harrison J.R., Federici F. and Ryan P. 2022 *Nucl. Mater. Energy* **33** 101278
[46] Fil A., Lipschultz B., Moulton D., Thornton A., Dudson B.D., Myatra O. and Verhaegh K. (the EUROfusion MST1 Team) 2022 *Nucl. Fusion* **62** 096026
[47] Moulton D. *et al* 2024 *Nucl. Fusion* **64** 076049
[48] Verhaegh K. *et al* 2023 *Nucl. Fusion* **63** 016014
[49] Myatra O., Lipschultz B., Moulton D., Verhaegh K., Dudson B., Orchard S., Fil A. and Cowley C. 2023 *Nucl. Fusion* **63** 096018
[50] Cowley C., Lipschultz B., Moulton D. and Dudson B. 2022 *Nucl. Fusion* **62** 086046
[51] Verhaegh K. *et al* 2024 *Nucl. Fusion* **64** 086050
[52] Verhaegh K. *et al* 2023 *Nucl. Fusion* **63** 076015

[53] Myatra O., Moulton D., Dudson B., Lipschultz B., Newton S., Verhaegh K. and Fil A. 2023 *Nucl. Fusion* **63** 076030

[54] Soukhanovskii V.A., Khrabry A.I., Scott H.A., Rognlien T.D., Moulton D. and Harrison J.R. 2022 *Nucl. Fusion* **62** 066047

[55] Penaflor B.G. 1996 *Fusion Technol.* pp 965–8

[56] McArdle G., Pangione L. and Kochan M. 2020 *Fusion Eng. Des.* **159** 111764

[57] Kochan M. *et al* 2023 *30th IEEE Symp. on Fusion Eng.* (*Oxford, UK*, *9–13 July 2023*) (available at: https:// sofe2023.co.uk/)

[58] Anand H., Eldon D., Kochan M., McArdle G., Pangione L. and Wang H.Q. 2022 *Fusion Eng. Des.* **177** 113086

[59] Anand H. *et al* 2024 *Nucl. Fusion* **64** 086051

[60] O'Gorman T., Naylor G., Scannell R., Cunningham G., Brunner K.J., Martin R. and Croft D. 2014 *Rev. Sci. Instrum.* **85** 11D861

[61] Kardaun O. 1999 *Plasma Phys. Control. Fusion* **41** 429

[62] Havlíčková E., Harrison J., Lipschultz B., Fishpool G., Kirk A., Thornton A., Wischmeier M., Elmore S. and Allan S. 2015 *Plasma Phys. Control. Fusion* **57** 115001

[63] Wilson H.R. *et al* 2020 STEP—on the pathway to fusion commercialization *Commercialising Fusion Energy* (IOP Publishing) pp 8-1–8-18

[64] Loarte A. and Neu R. 2017 *Fusion Eng. Des.* **122** 256–73

[65] Siccinio M. *et al* 2020 *Fusion Eng. Des.* **156** 111603

[66] Militello F. *et al* 2021 *Nucl. Mater. Energy* **26** 100908

[67] Kaye S.M., Connor J.W. and Roach C.M. 2021 *Plasma Phys. Control. Fusion* **63** 123001

[68] Kennedy D., Giacomin M., Casson F.J., Dickinson D., Hornsby W.A., Patel B.S. and Roach C.M. 2023 *Nucl. Fusion* **63** 126061